Non-linear homogenization of polymer composites with porous inclusions

D Zeka, A Catapano, P Mariano, M Montemurro, R Poupart, O Mondain-Monval, J Delcroix, P Rublon

Non-linear homogenization of polymer composites with porous inclusions

D. Zeka[a,b], A. Catapano[b], P. M. Mariano[a], M. Montemurro[c], R. Poupart[d], O. Mondain-Monval[d], J. Delcroix[e], P. Rublon[e]

[a] *DICEA, Università di Firenze*
via Santa Marta 3, I-50139 Firenze, Italy
e-mail: paolomaria.mariano@unifi.it
e-mail: donald.zeka@stud.unifi.it

[b] *Bordeaux INP, Université de Bordeaux, Arts et Métiers Institute of Technology, CNRS, INRA, ENSAM Université*
I2M UMR 5295, F-33405 Talence, France
e-mail: anita.catapano@bordeaux-inp.fr

[c] *Arts et Métiers Institute of Technology, Université de Bordeaux, CNRS, INRA, Bordeaux INP, HESAM Université*
I2M UMR 5295, F-33405 Talence, France
e-mail: marco.montemurro@ensam.eu

[d] *University of Bordeaux, CNRS, UMR 5031, Centre de Recherche Paul Pascal*
F-33600 Pessac, France
e-mail: romain.poupart@crpp.cnrs.fr
e-mail: olivier.mondain@crpp.cnrs.fr

[e] *Naval Group Research, Centre d'Expertise des Structures et Matériaux Navals (CESMAN), Technocampus Océan*
5 Rue de l'Halbrane, 44340 Bouguenais, France
e-mail: julien-a.delcroix@naval-group.com
e-mail: pierre.rublon@naval-group.com

Abstract

We homogenize the mechanical properties of a two-phase polymer composite, made of a polyurethane matrix containing porous spherical silicone-based inclusions, and designed to be used for wave control as a local resonant insulator. First we consider a homogenized energy for the spherical inclusions, an expression obtained by an explicit method. Then, we couple inclusions and matrix by means of the second-order tangent method. Direct finite element simulations allow some comparisons with available experiments.

Key words: Homogenization; Multiscale modelling; Hyperelasticity; Metamaterials; Finite elements.

1 Introduction

Physical properties of composites depend on several factors: nature and volume fractions of the constituents, size and shape of the inclusions, matrix-inclusion interface properties, etc. A comprehensive review concerning the effects of particle size, particle-matrix interface adhesion and particle-loading on the stiffness, strength and toughness of such particulate polymer composites is in reference [56] (see also [72,31,62,65,16,70,54,63,55]).

Pertinent homogenization techniques are manifold (see, e.g., [20,11,44,33]). They cover even non-linear constitutive structures [68,66,67] and large strain setting [26,27,45]. The treatise by G. Milton [43] represents a good literature review on the topic.

Related computational techniques rest on the solution of two nested boundary problems, one at the macroscopic scale, the other at a microscopic scale, the one of heterogeneities [34] (see also, e.g., [17,42]). A starting point is the evaluation of the macroscopic deformation gradient at every integration point. This allows assigning Dirichlet-type boundary conditions to a statistically representative volume element (SRVE). Once equilibrium for the SRVE has been determined, the macroscopic stress follows as an average of the SRVE stress field. In this way, we can consider large strains at both gross and sub-SRVE scales. Although the computational cost is lower with respect to the one of a full scale simulation, the approach is still computationally cumbersome, since it requires the solution of a wide set of non-linear problems.

Analytical and semi-analytical approaches to homogenization are mainly restricted to specific microstructural arrangements in linear elastic range; some results in the presence of large strains and elastic behavior are also available under particular loading conditions [43,59] (for appropriate bounds to geometrically non-linear composites see [46,47]). However, also in this case, the homogenization strategy could require the numerical resolution of a set of non-linear equations.

A way to estimate the effective elastic behavior of heterogeneous materials in non-linear setting rests on a truncated expansion of the elastic energy density with respect to the deformation gradient (as introduced in reference [49]; see also [52]). Here, we follow this path to homogenize a particle-based composite consisting of porous silicone microspheres embedded in a polyurethane (PU) matrix. Two scales need to be considered: the microscopic one pertaining to each porous sphere (in which two phases can be identified: silicone-rubber and voids), and the scale involving PU matrix and spheres taken after their own

homogenization.

The material we are interested in is commonly used as an acoustic insulator. Indeed, such a composite can be designed to get extreme acoustic macroscopic properties, such as large, small, imaginary or negative index of refraction [20,11,44,33]. Locally resonant composites are designed, in fact, to optimize the spatial wave-control with a sub-wavelength architecture of small inclusions distributed (uniformly or not) in an appropriate matrix. They help in reaching underwater furtivity of submarines from sonars, obtained by a sound-absorbing coating, designed to reduce both the reflection of incident waves and their transmission properties. In fact, PU matrices exhibit a low reflection coefficient with respect to liquids like water [57] (see also [64,73]). To improve the internal damping properties of the polymer, thus the ability to dissipate acoustic wave energy, different types of inclusions can be considered, e.g. glass spheres, nanographene and, more commonly, hollow spherical shells, also called micro-balloons [5,38]. Elastomers characterized by porosities of about 1-10 μm have also been used for the fabrication of locally resonant composites [53,4]. Their modulus of compressibility (i.e., the sound speed inside them) strongly depends on a small fraction of pores (this is mainly due to the very low shear modulus of the matrix). Then, we can create spherical Mie-type resonators at low frequency (Figure 1) to be dispersed in the PU matrix (see also [8,7,53]).

The locally resonant composite considered here has been variously discussed in references [8,7,53], where it has been shown how control over the porous bead size allows the selection of a frequency range in which the composite exhibits a prominent acoustic attenuation. For a deeper insight into the matter on the main advantages in using a three-phase composite instead of classical soft acoustic insulators solutions available in literature the reader is addressed to [7,8].

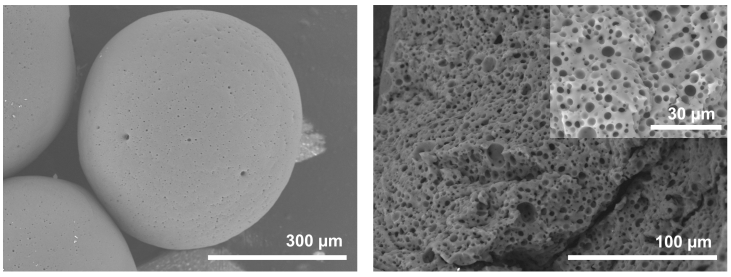

Figure 1. Porous elastomeric microspheres (left: a single spherical resonator; right: porous structure with a close-up inserted). Pictures taken with an Hitachi TM-1000 apparatus; the samples have been previously metallized with a thin layer of Pt.

Here, we neither dwell upon specific applications nor consider inertial effects, so that we exclude a direct analysis of the acoustic behavior. We limit ourselves

to the homogenization of elastic material properties of such a composite. Since the inclusions have no degrees of freedom that are relative to the matrix, we do not need to exploit directly the general model-building framework for the mechanics of complex materials (see [39]), so that our result is an "equivalent" Cauchy-type body. Therefore this work can be placed in the following context with respect to the acoustic application of the composite: the homogenization of the mechanical behavior due to a pre-stress state of the material, e.g. the hydrostatic pressure of the water surrounding the submarine.

This paper is organized as follows: in Section 2 we summarize a strategy for non-linear homogenization of hyperelastic media and specify how we use it. Section 3 collects details on the analytical homogenization. Pertinent results are in Section 4, while Section 5 reports comparisons with finite element (FE) analyses. Section 6 includes final remarks.

2 Elements of non-linear homogenization of hyperelastic media

A key point in homogenization methods is the choice of a material elementary cell whose properties are eventually attributed to a material point. Defining such a cell has not always a unique and immediate way [29]. For heterogeneous media with a periodic microstructure the definition of a representative volume element (RVE) is straightforward. Material heterogeneity complicates even enormously the analysis unless we recognize a spatial scale (which can be even not unique) at which we can consider the material to have a statistically periodical structure. The presence of at least one such a scale justifies the notion of SRVE (see also [24,13,28,41,40]). Roughly speaking, the characteristic size of the SRVE should be chosen in such a way that the distribution of the inclusions within the SRVE can be considered statistically self-similar (also referred to as "statistically periodic"). This means that, if one considers an SRVE of the same size located at a different region of the heterogeneous medium, the distribution of inclusions will be the same (although their position could be different). Under these circumstances, the equivalent homogenised properties of the continuum at the macroscopic scale will not depend upon the position of the SRVE into the heterogeneous medium. For a deeper insight into the matter the reader is addressed to [29].

Here, we consider the SRVE of a hyperelastic composite as made up of N phases, i.e., matrix and $N-1$ different types of inclusions randomly distributed. We also assume that the scales separation condition is fulfilled and that the SRVE undergoes homogeneous strain at its boundary. Consequently, the imposed deformation gradient $\overline{\mathbf{F}}$ is such that $\overline{\mathbf{F}} = \langle \mathbf{F} \rangle$, where $\mathbf{F}$ is the deformation gradient tensor inside the SRVE and $\langle \cdot \rangle$ indicates average over the SRVE. Inclusions and matrix are both assumed to be hyperelastic, each

one with pertinent objective elastic energy density $W^{(r)}(\mathbf{F}), r = 1, ..., N$, while the one pertaining to the SRVE is given by

$$W(\mathbf{x}, \mathbf{F}) = \sum_{r=1}^{N} \theta^{(r)}(\mathbf{x}) W^{(r)}(\mathbf{F}),$$

where $\theta^{(r)}(\mathbf{x})$ is the characteristic function of phase r (it is equal to 1 if the material point at $\mathbf{x}$ in the reference configuration belongs to the phase r, zero otherwise). The first Piola–Kirchhoff stress tensor $\mathbf{P}$ at $\mathbf{x}$ in the SRVE is given by

$$\mathbf{P} = \frac{\partial W(\mathbf{x}, \mathbf{F})}{\partial \mathbf{F}}.$$

The effective internal (strain) energy density $\widetilde{W}$ is defined by

$$\widetilde{W}(\overline{\mathbf{F}}) := \min_{\mathbf{F} \in \mathscr{K}(\overline{\mathbf{F}})} \langle W(\mathbf{x}, \mathbf{F}) \rangle = \min_{\mathbf{F} \in \mathscr{K}(\overline{\mathbf{F}})} \sum_{r=1}^{N} c^{(r)} \langle W^{(r)}(\mathbf{F}) \rangle^{(r)}, \tag{2.1}$$

where $c^{(r)}$ is the volume fraction of phase r, $\langle \cdot \rangle^{(r)}$ indicates the average over the phase r, while $\langle \cdot \rangle$ is once again the SRVE average, where the spatial variable $\mathbf{x}$ in the term defining $\widetilde{W}(\overline{\mathbf{F}})$ ranges. The minimum is taken over the set $\mathscr{K}(\overline{\mathbf{F}})$ of kinematically admissible deformation gradients. Finally, according to a proposal by R. Hill [26], the effective stress in the composite $\overline{\mathbf{P}} = \langle \mathbf{P} \rangle$ is related to the macroscopic deformation gradient $\overline{\mathbf{F}} = \langle \mathbf{F} \rangle$ through

$$\overline{\mathbf{P}} = \frac{\partial \widetilde{W}(\overline{\mathbf{F}})}{\partial \overline{\mathbf{F}}}. \tag{2.2}$$

2.1 Microscopic-mesoscopic scale transition: explicit strain energy densities for porous elastomers

Silicone rubber may be considered as incompressible because its stiffness under compression is definitely higher than the shear one [4]. A neo-Hookean type energy density, namely

$$W(\mathbf{F}) := \begin{cases} \frac{\mu}{2}(I_1 - 3) & \text{if } \det(\mathbf{F}) = 1, \\ +\infty & \text{otherwhise,} \end{cases}$$

where μ is the shear modulus and $I_1 := \mathrm{tr}(\mathbf{C})$, with $\mathbf{C} := \mathbf{F}^T\mathbf{F}$ the right Cauchy-Green tensor, appears to be appropriate for it. However such a choice does not account for porosity of the spheres that we consider, so we start homogenizing the spherical inclusion.

Be f_0 the void volume fraction (porosity) in the silicone matrix. Its presence has two effects: (1) the homogenized continuum will be characterized by elastic

moduli lower than those of the elastomer; (2) the incompressibility assumption will no longer apply.

Several attempts with different methods have been made to homogenize porous elastomers, e.g. [30,6]. In 1962, P. J. Blatz and W. L. Ko [6] proposed a strain energy density expression, corroborated by experimental results on PU porous rubber:

$$W(\mathbf{F}) = \frac{1}{2}\mu f(I_1 - 1 - \frac{1}{\nu} + \frac{1-2\nu}{\nu} J^{\frac{-2\nu}{1-2\nu}}) + \frac{1}{2}\mu(1-f)(\frac{I_2}{J^2} - 1 - \frac{1}{\nu} + \frac{1-2\nu}{\nu} J^{\frac{2\nu}{1-2\nu}}),$$

where μ and ν correspond, respectively, to shear modulus and Poisson's ratio in small strain regime, f is a material parameter to be determined by a data fitting procedure, $J := \det(\mathbf{F})$ and $I_2 := \frac{1}{2}[(\mathrm{tr}(\mathbf{C}))^2 - \mathrm{tr}(\mathbf{C}^2)]$. Simple tension, strip-biaxial tension, and homogeneous-biaxial tension tests of a 47% foamed PU rubber were at the ground of that proposal. In a similar way, in [30], a phenomenological approach based on the invariants of the logarithmic strain is proposed for the constitutive modelling of PU-based elastomer foam. However, these approaches require proper fitting of the material parameters through various experimental tests, which are not available in our case.

A first explicit approximate result for arbitrary large strains is due to M. Danielsson, D.M. Parks, and M.C. Boyce [12]; it is an upper bound for the actual behavior of incompressible porous hyperelastic materials with HSA microstructure, obtained by making use of appropriate kinematically admissible fields on a hollow elastomeric sphere.

Under large strain conditions, O. Lopez-Pamies and P. Ponte-Castañeda got [35,36] more accurate estimates than those reported in reference [12]. Their result, however, is implicit and requires the numerical resolution of a system including seven non-linear algebraic equations.

Eventually, B. Shrimali, V. Lefevre, and O. Lopez-Pamies [58] proposed an approximated explicit solution for the effective strain energy density of porous neo-Hookean incompressible elastomers, which holds for isotropic distributions of empty pores. It reads

$$\begin{aligned}\widetilde{W}(\mathbf{F}, f_0) =& \frac{3(1-f_0)\mu}{2(3+2f_0)}[I_1 - 3] \\ &+ \frac{3\mu}{2J^{1/3}}\left[2J - 1 - \frac{(1-f_0)J^{1/3}(3J^{2/3}+2f_0)}{3+2f_0}\right. \\ &\left. - \frac{f_0^{1/3}J^{1/3}(2J+f_0-2)}{(J-1+f_0)^{1/3}}\right],\end{aligned} \tag{2.3}$$

where μ is the shear modulus of the incompressible matrix while f_0, J, and I_1 have been above defined. Such an expression of the energy accurately de-

scribes the mechanical behavior of the porous body regardless the shape and dispersion of pores and for a maximum value of the initial void volume fraction equal to 30%, which corresponds to our range of interest.

Based on the above considerations, we take the energy (2.3) as an appropriate form for the porous silicone spheres with randomly distributed pores, whose characteristic diameter varies between 0 μm and 10 μm.

The standard condition for elastic simple bodies, which prescribes that the energy grows up to infinity when the determinant of $\mathbf{F}$ goes to zero (see treatises as [60]), for the energy density (2.3) changes into

$$\lim_{J\to 1-f_0} \widetilde{W}(\mathbf{F}, f_0) = +\infty\,. \tag{2.4}$$

Remark 2.1 *The main drawback in the choice of* (2.3) *is an overestimation of the stiffness when volumetric strain grows. Nevertheless, for lower values, the predicted behavior appears to be sufficiently accurate for our purposes.*

2.2 The second-order method

Overview

The second-order method, introduced by P. Ponte-Castañeda [49], and later applied to hyperlastic composites [52], provides estimates for the effective elastic energy density (2.1). It rests on a truncation at second order of the Taylor expansion for the elastic energy densities $W^{(r)}(\mathbf{F})$ of the underlying phases:

$$W^{(r)}(\mathbf{F}) \approx W^{(r)}(\mathbf{F}^{(r)}) - \mathbf{P}^{(r)}\cdot\mathbf{F}^{(r)} + \frac{1}{2}\mathbf{F}^{(r)}\cdot\overline{\mathbb{L}}^{(r)}\mathbf{F}^{(r)} + \boldsymbol{\tau}^{(r)}\cdot\mathbf{F} + \frac{1}{2}\mathbf{F}\cdot\overline{\mathbb{L}}^{(r)}\mathbf{F}, \tag{2.5}$$

where $\mathbf{F}^{(r)}$ is an unknown reference deformation gradient, assumed to be uniform in each phase. The tensor $\mathbf{P}^{(r)} = \dfrac{\partial W^{(r)}}{\partial \mathbf{F}}(\mathbf{F}^{(r)})$ is the first Piola-Kirchhoff stress in the r-th phase evaluated at $\mathbf{F}^{(r)}$, while $\boldsymbol{\tau}^{(r)} = \mathbf{P}^{(r)} - \overline{\mathbb{L}}^{(r)}\mathbf{F}^{(r)}$, whereas $\overline{\mathbb{L}}^{(r)}$ is a fourth-rank tensor to be determined.

By inserting equation (2.5) into (2.1), we get

$$\widetilde{W}(\overline{\mathbf{F}}) = \min_{\mathbf{F}^{(r)},\overline{\mathbb{L}}^{(r)}} \left(\sum_{r=1}^{N} c^{(r)} \Big(W^{(r)}(\mathbf{F}^{(r)}) - \mathbf{P}^{(r)}\cdot\mathbf{F}^{(r)} + \frac{1}{2}\mathbf{F}^{(r)}\cdot\overline{\mathbb{L}}^{(r)}\mathbf{F}^{(r)} \Big) \right) + \widehat{W}(\overline{\mathbf{F}}),$$

where $\widehat{W}(\overline{\mathbf{F}})$ is defined as

$$\widehat{W}(\overline{\mathbf{F}}) := \min_{\mathbf{F}\in\mathscr{K}(\overline{\mathbf{F}})} \Big\langle \boldsymbol{\tau}(\mathbf{x})\cdot\mathbf{F} + \frac{1}{2}\mathbf{F}\cdot\mathbb{L}_0(\mathbf{x})\mathbf{F}\Big\rangle. \tag{2.6}$$

It represents the effective free energy density of a fictitious linear 'thermoelastic' composite, having reference configuration and microstructure as the original hyperelastic material, subjected to the same macroscopic deformation, with stiffness tensor

$$\mathbb{L}_0(\mathbf{x}) = \sum_{r=1}^{N} \theta^{(r)}(\mathbf{x})\overline{\mathbb{L}}^{(r)},$$

and 'thermal' stress tensor

$$\boldsymbol{\tau}(\mathbf{x}) = \sum_{r=1}^{N} \theta^{(r)}(\mathbf{x})\boldsymbol{\tau}^{(r)}.$$

To estimate the macroscopic strain energy density of the non-linear hyperelastic composite, the associated linear 'thermoelastic' boundary value problem must be solved.

The choice of $\mathbf{F}^{(r)}$ and $\overline{\mathbb{L}}^{(r)}$ needs to be specified. According to reference [52], the deformation gradients $\mathbf{F}^{(r)}$ are given by

$$\mathbf{F}^{(r)} = \langle \mathbf{F}\rangle^{(r)} =: \overline{\mathbf{F}}^{(r)},$$

with $\mathbf{F}$ the argument minimizing (2.6). Tensors $\overline{\mathbb{L}}^{(r)}$, instead, are taken equal to the hyperelastic phase tangent modulus, namely,

$$\overline{\mathbb{L}}^{(r)} = \mathbb{L}^{(r)}(\overline{\mathbf{F}}^{(r)}) := \frac{\partial^2 W^{(r)}}{\partial\mathbf{F}\partial\mathbf{F}}(\overline{\mathbf{F}}^{(r)}). \tag{2.7}$$

The resulting effective elastic energy density reads

$$\widetilde{W}(\overline{\mathbf{F}}) = \sum_{r=1}^{N} c_r\left[W^{(r)}(\overline{\mathbf{F}}^{(r)}) + \frac{1}{2}\mathbf{P}^{(r)}(\overline{\mathbf{F}}^{(r)})\cdot(\overline{\mathbf{F}} - \overline{\mathbf{F}}^{(r)})\right]. \tag{2.8}$$

Remark 2.2 *Different choices can be made for the fourth-rank linear operators $\overline{\mathbb{L}}^{(r)}$; for example, they can be chosen as secant moduli instead of the tangent ones, or we can include possible fluctuations in their definition, as done in references [50,51].*

Application to two-phase composites with porous spherical inclusions

In the special case that we treat here, wherein deformable spherical porous particles (phase "2") are randomly scattered in an elastic matrix (phase "1"),

we compute $\overline{\mathbf{F}}^{(1)}$ and $\overline{\mathbf{F}}^{(2)}$ by determining the minimum (2.6) associated with the linear 'thermoelastic' comparison composite subjected to a macroscopic deformation gradient $\overline{\mathbf{F}}$.

By exploiting a result due to V. T. Levin [32], we obtain

$$\overline{\mathbf{F}}^{(r)} = \mathbb{A}^{(r)}\overline{\mathbf{F}} + (\mathbb{A}^{(r)} - \mathbb{I})(\Delta\mathbb{L})^{-1}(\Delta\boldsymbol{\tau}), \quad r = 1, 2, \tag{2.9}$$

where $\Delta\mathbb{L} := \mathbb{L}^{(1)}(\overline{\mathbf{F}}^{(1)}) - \mathbb{L}^{(2)}(\overline{\mathbf{F}}^{(2)})$ and $\Delta\boldsymbol{\tau} := \boldsymbol{\tau}^{(1)}(\overline{\mathbf{F}}^{(1)}) - \boldsymbol{\tau}^{(2)}(\overline{\mathbf{F}}^{(2)})$. In equation (2.9), $\mathbb{A}^{(r)}$ represents the strain localization tensor of phase r in the linear elastic case; $\mathbb{A}^{(r)}$, with $r = 1, 2$, is such that

$$c^{(1)}\mathbb{A}^{(1)} + c^{(2)}\mathbb{A}^{(2)} = \mathbb{I},$$

with $\mathbb{I}$ the fourth-rank unit tensor. We recall that the actual expression of the localization tensor depends on the chosen linear homogenization scheme, and allows us to generate the corresponding non-linear estimates for $\widetilde{W}$.

Generalized Hashin-Shtrikman estimates for the localization tensors [22] have been given by Willis [68], see also Castaneda and Tiberio [52]. For the special case of two-phase composites with particulate microstructure, the expressions of the localization tensors are the following ones:

$$\mathbb{A}^{(1)} = [c^{(1)}\mathbb{I} + c^{(2)}[\mathbb{I} - \mathbb{P}\Delta\mathbb{L}]^{-1}]^{-1},$$
$$\mathbb{A}^{(2)} = [\mathbb{I} - c^{(1)}\mathbb{P}\Delta\mathbb{L}]^{-1},$$

where $\mathbb{P}$ represents the Hill tensor associated with the matrix-inclusion problem, according to Eshelby's theory [15,25]. It should be pointed out that previous expressions of localization tensors were derived in the context of linear elasticity with pertinent symmetric strain and stress tensors as well as with elasticity tensors showing major and minor symmetries. However, as explained in [52], these results apply even in the case considered here, i.e. non-symmetric strain and stress tensors and elasticity tensor showing only major symmetries. By assuming that the spherical particles are randomly dispersed in the matrix, and that the composite is statistically isotropic in the reference configuration, Hill's tensor reads

$$\mathbb{P} = \mathbb{P}^{(1)} = \frac{1}{4\pi}\int_0^{2\pi}\int_0^{\pi} \mathbb{H}^{(1)}(\xi)\sin\Phi \mathrm{d}\Phi\mathrm{d}\Theta, \tag{2.10}$$

with

$$\mathbb{H}^{(1)}_{ijkl}(\xi) = \mathbf{N}^{(1)}_{ik}\xi_j\xi_l \ ,$$
$$\mathbf{N}^{(1)} = \left(\mathbf{K}^{(1)}\right)^{-1} \ ,$$
$$\mathbf{K}^{(1)}_{ik} = \mathbb{L}^{(1)}_{ijkl}\xi_j\xi_l \ ,$$

where $\xi_1 = \cos\Theta \sin\Phi$, $\xi_2 = \sin\Theta \cos\Phi$, $\xi_3 = \cos\Phi$. The assessment of Hill's tensor (which is not symmetric in the present case) requires the integration of its 81 components over the unit sphere.

The homogenization process reduces to the analysis of a non-linear system (2.9) for the nine components of $\overline{\mathbf{F}}^{(1)}$ and $\overline{\mathbf{F}}^{(2)}$, which allows us to evaluate the effective elastic energy $\widetilde{W}$, according to equation (2.8).

3 Implementation of the second-order homogenization method

The implementation of what we have above summarized requires the definition of suitable elastic energy densities for matrix and inclusions, an effective strategy to solve the non-linear system (2.9), the numerical evaluation of the effective stress (2.2).

3.1 Material properties of the constitutive phases

We refer to composites consisting of a dispersion of porous silicone microspheres, with a diameter greater than 100 μm, in a PU matrix (see also [53]). The PU matrix is a bi-component commercial polyurethane, provided by Sika [61]. It is made of a polyol solution (Part B) and an isocyanate mixture (Part A). Each microsphere is made of Silcolease UV Cata221 TM and an epoxy-bearing PDMS rubber (Silcolease UV Poly200 TM), provided by Elkem [14]. An emulsion process allows one to obtain the microspheres in two steps. The first one exploits microfluidics and allows synthesising spheres of controlled diameter and porosity. The inverse emulsion (W/O) rest on the use of a syringe pump under a controlled flux of glycerol. Polymerization follows while droplets flow-through. The second step consists of a double emulsion approach (W/O/W), which allows us to produce a large quantity of spheres, even though they are characterized by a higher diameter dispersion (see Table 1).

Label	Type	Spheres size
A	Monodisperse	192±25 μm
B	Monodisperse	338±32 μm
C	Monodisperse	505±40 μm
D	Polydisperse	203±110 μm

Table 1
Size values of the porous elastomeric spheres exploited in reference [53].

For the PU matrix, experimental data from confined compression tests realized at Naval Group are available, together with indicative values for the shear modulus in small strain regime. Reference samples of pure PU were fabricated by mixing together $5g$ of polyol B and $10g$ of isocyanate A. Tests under confined uni-axial cyclic compression on cylindrical specimens (see Fig. 2) with diameter and height of $30mm$ allows sample characterization. The specimen fills a rigid cylindrical recipient with radius of $30mm$. A ZwickRoell Z005 machine at cross-head speed of $200mm/min$ develops the test. A ZwickRoell long-stroke extensometer allows strain measures. The stress-strain curve un-

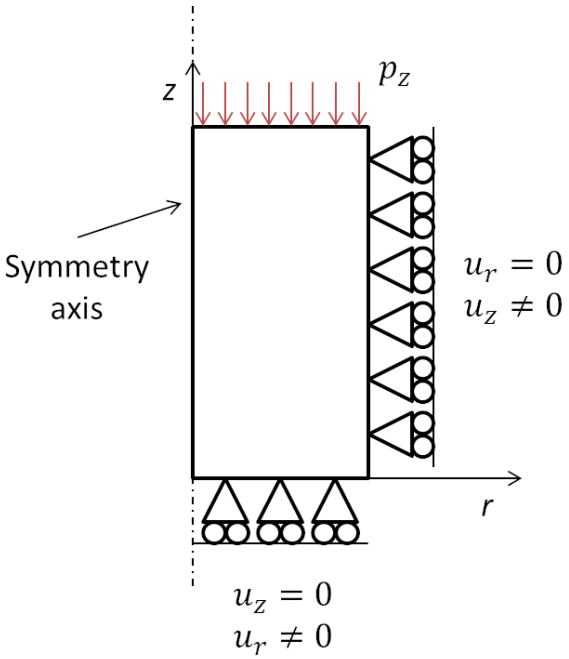

Figure 2. Schematic boundary conditions on experimental confined compression tests: axial-symmetric conditions.

der confined compression conditions (Figure 3) shows almost vanishing initial slope, followed by a sudden increase. The neo-Hookean (or Mooney-Rivlin) scheme, which presumes a linear trend of stress with respect to volumetric strain, appears to be not suitable due to the evidences that we have. At variance, a second-order Yeoh's polynomial form for the elastic energy of the matrix seems to be more adequate to describe that behavior, so that we choose [69]

$$W^{(1)}(\mathbf{F}) = \sum_{p=1}^{2} C_{p0}(i_1 - 3)^p + \sum_{k=1}^{2} D_k(J-1)^{2k},$$

where $i_1 = I_1 J^{-2/3}$ is the first deviatoric invariant. Values of the material constants C_{p0} and D_k are intended to emerge from a data fitting approach. However, the limited set of experimental data does not guarantee that a simple parameter-tuning strategy could give physically significant results. For this reason we set-up these parameters on the basis of mechanical considerations. In

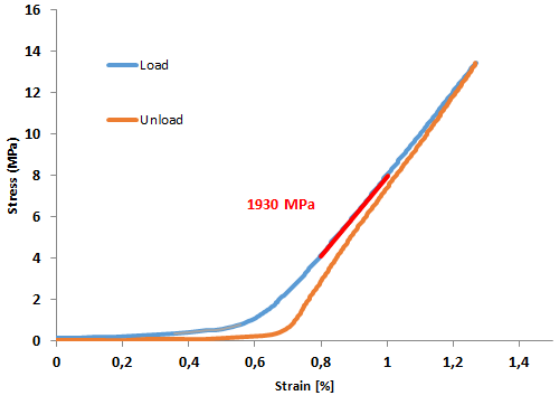

Figure 3. Confined compression test on pure PU.

small strain regime, in fact, to be consistent with the linear theory of elasticity, we should have $C_{10} = \frac{\mu}{2}$ and $D_1 = \frac{K}{2}$, with μ and K being, respectively, shear and compressibility moduli. For the initial shear modulus of the PU, a reference value of 5 MPa, which is typical of PU rubbers, has been chosen. We set equal to zero the parameter C_{20}, instead, in order to neglect higher-order dependence of the elastic energy density on the deviatoric strain. In fact, under confined state, the PU undergoes volumetric compression and, thus, the elastic energy associated with volume variation is dominant. We choose also D_1 equal to zero, because it roughly corresponds to the initial slope of the stress-strain curve in Figure 3. Also, we set D_2 equal to the slope in Figure 3, i.e., about 2000 MPa.

In order to check the adequacy of the chosen parameters, we performed a curve fitting MATLAB-based analysis in which, to obtain physically meaningful values of the parameters, we have been forced in a sense to set C_{20} equal to zero. Table 2 summarizes the comparison with our initial choices.

As shown in Figure 4, there is no significant difference between the two curves: this means that the expression of the strain energy density for the PU represents a reasonable approximation of the experimental curve obtained under confined compression, at least up to 1% of strain. Moreover, we can employ such an approximation because the PU strain state in the composite does not exceed this value in the application considered here.

Nevertheless, it is difficult to assess the influence of using this strain energy density of the PU matrix as an input in the homogenization properties of the whole composite submitted to confined compression. Indeed, when the confined compression holds for the whole composite material, due to interactions between the PU matrix and the porous spheres, the curve of Figure 3 does not apply everywhere into the PU matrix.

In what follows we base our analyses only on the values of parameters in Table 2, those chosen through mechanical considerations.

Criterion	C_{10}	C_{20}	D_1	D_2
mechanical considerations	2.5	0	0	2×10^6
MATLAB	3.44	0	1.17×10^{-6}	1.91×10^6

Table 2
Material parameters for the PU matrix (values in MPa).

The material properties of the porous spherical inclusions are listed in Table 3. Those data are taken from [4] and concern only shear and compressibility moduli in small strain regime. f_0, on the other hand, correspond to the actual porosity volume fraction of silicone beads. Figure 5 shows the resulting stress-volumetric strain curve for the porous microspheres under hydrostatic compression. For volumetric strain close to 30% (which corresponds to the void volume fraction), the predicted stress tends to infinity, because the matrix is assumed to be incompressible. Indeed, for strain close to this value, the curve should be proportional to the compressibility modulus of the silicone elastomer. On the other hand, for lower values of the volumetric strain, the explicit effective energy density guarantees reliable results.

μ (MPa)	f_0
0.3 [4]	0.3

Table 3
Material parameters used for the strain energy density of the porous inclusions.

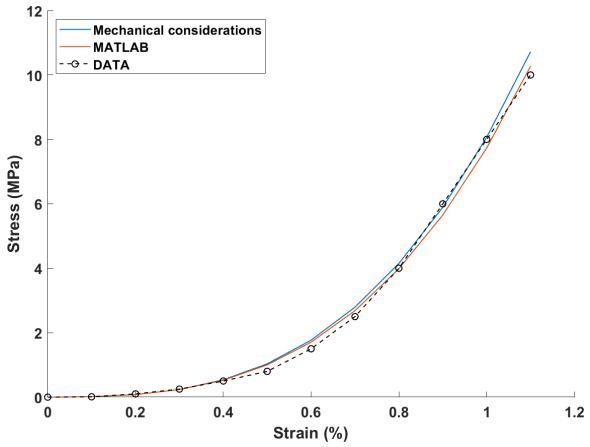

Figure 4. Comparison between experimental data of pure PU and the interpolating curves.

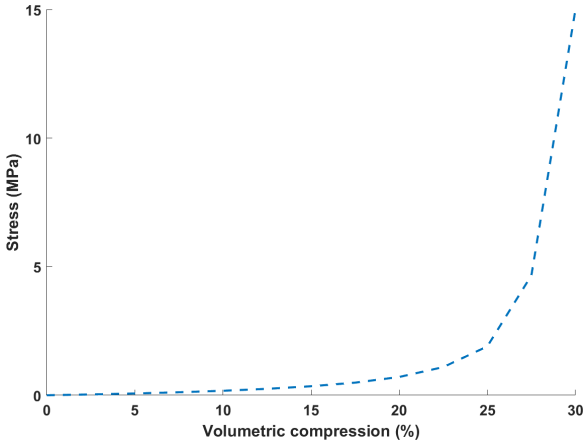

Figure 5. Stress as a function of the volume variations for (2.3) when using parameters of Table 3 under hydrostatic compression.

3.2 Numerical strategy

As already stated, the evaluation of effective elastic energy of the composite requires the analysis of the non-linear system (2.9). To this aim we use an effective resolution algorithm. Specifically, Algorithms 1 and 2, specified here below, are the pseudo-code for solving the non-linear system (2.9) and computing the effective elastic energy density (2.8), while Algorithm 3 is a pseudo-code for computing the first Piola-Kirchoff tensor.

For the confined compression macroscopic state characterization, we consider an uniaxial homogeneous strain in the specimen. Specifically, we chose

$$\overline{\mathbf{F}} = \overline{\lambda}\mathbf{e}_1 \otimes \mathbf{e}_1 + \mathbf{e}_2 \otimes \mathbf{e}_2 + \mathbf{e}_3 \otimes \mathbf{e}_3, \tag{3.1}$$

with $\overline{\lambda} < 1$ and $\mathbf{e}_1$ being the unit vector along the compression direction; $\mathbf{e}_2$ and $\mathbf{e}_3$ constitute with $\mathbf{e}_1$ an orthonormal frame.

In the case of a two-phase material, it is thus sufficient to determine only $\overline{\mathbf{F}}^{(1)}$, the tensor $\overline{\mathbf{F}}^{(2)}$ emerges from the relation

$$\overline{\mathbf{F}} = c^{(1)}\overline{\mathbf{F}}^{(1)} + c^{(2)}\overline{\mathbf{F}}^{(2)}. \tag{3.2}$$

The system (2.9) involves nine non-linear equations, which correspond to the nine components of $\overline{\mathbf{F}}^{(1)}$:

$$\overline{\mathbf{F}}^{(1)} = \mathbb{A}^{(1)}\overline{\mathbf{F}} + (\mathbb{A}^{(1)} - \mathbb{I})(\mathbb{L}^{(1)} - \mathbb{L}^{(2)})^{-1}(\boldsymbol{\tau}^{(1)} - \boldsymbol{\tau}^{(2)}). \tag{3.3}$$

Thus, for its analysis, a fixed-point iteration scheme appears a useful strategy.

By taking into account the sensitivity to initial guess of non-linear systems, for the analysis developed here we set the initial value of $\overline{\mathbf{F}}^{(1)}$ equal to the macro-

scopic deformation gradient $\overline{\mathbf{F}}$ because the matrix is considerably stiffer than the inclusions, so its strain does not significantly differ from the macroscopic one.

Algorithm 1 FixedPoint [ ]: fixed point iteration scheme

Input: $\overline{\mathbf{F}}$
Initialize $\overline{\mathbf{F}}^{(1)} = \overline{\mathbf{F}}$
Compute residual $\mathbf{r} = \texttt{RHS}[\overline{\mathbf{F}}^{(1)}, \overline{\mathbf{F}}] - \overline{\mathbf{F}}^{(1)}$
procedure WHILE($\|\mathbf{r}\| > tol$) **do**
  Update $\overline{\mathbf{F}}^{(1)} \leftarrow\texttt{RHS}[\overline{\mathbf{F}}^{(1)}, \overline{\mathbf{F}}]$
  Compute new residual $\mathbf{r} = \texttt{RHS}[\overline{\mathbf{F}}^{(1)}, \overline{\mathbf{F}}] - \overline{\mathbf{F}}^{(1)}$
end procedure
Compute $\overline{\mathbf{F}}^{(2)}$ from Eq. (3.2)
Evaluate $\widetilde{W}(\overline{\mathbf{F}})$ from Eq. (2.8)
Return: $\widetilde{W}(\overline{\mathbf{F}})$

Algorithm 2 RHS[ ]: evaluation of the right-hand side of Eq. (3.3)

Input: $\overline{\mathbf{F}}$, $\overline{\mathbf{F}}^{(1)}$
Compute $\overline{\mathbf{F}}^{(2)}$ from Eq. (3.2)
Evaluate $\boldsymbol{\tau}^{(1)}$ and $\mathbb{L}^{(1)}$ in $\overline{\mathbf{F}}^{(1)}$
Evaluate $\boldsymbol{\tau}^{(2)}$ and $\mathbb{L}^{(2)}$ in $\overline{\mathbf{F}}^{(2)}$
Integrate $\mathbb{P}$ from Eq. (2.10)
Compute $\mathbb{A}^{(1)}$ from Eq. (2.2)
Return: $\mathbb{A}^{(1)}\overline{\mathbf{F}} + (\mathbb{A}^{(1)} - \mathbb{I})(\mathbb{L}^{(1)} - \mathbb{L}^{(2)})^{-1}(\boldsymbol{\tau}^{(1)} - \boldsymbol{\tau}^{(2)})$

Algorithm 3 Effective stress computation

Input: $\overline{\mathbf{F}}$
procedure
  for $i = 1$ to 3 **do**
    for $j = 1$ to 3 **do**
      Define increments $\overline{\mathbf{F}}^{\pm} = \overline{\mathbf{F}} \pm \delta \mathbf{e}_i \otimes \mathbf{e}_j$
      Compute $\widetilde{W}(\overline{\mathbf{F}}^{\pm}) =$`FixedPoint`$(\overline{\mathbf{F}}^{\pm})$
      Compute homogenized stress $\overline{\mathbf{P}} = \dfrac{\widetilde{W}(\overline{\mathbf{F}}^{+}) - \widetilde{W}(\overline{\mathbf{F}}^{-})}{2\delta}$
    end for
  end for
end procedure
Return: $\overline{\mathbf{P}}$

By rendering isotropic the Hill tensor

In Algorithm 2, we evaluate the Hill tensor $\mathbb{P}$, required to compute $\mathbb{A}^{(1)}$, at every iteration, with a general purpose integration scheme available in Python. However, this task requires a significant computational effort at each iteration.

In order to speed up the calculation, it is possible to avoid the numerical integration by rendering isotropic the Hill tensor.

$\mathbb{P}$ depends only on inclusion geometry and tangent constitutive tensor $\mathbb{L}^{(1)}$ of the matrix; it can be equivalently expressed in terms of Eshelby's tensor $\mathbb{S}^E$ [15] as

$$\mathbb{P} = \mathbb{S}^E \mathbb{L}^{(1)^{-1}}.$$

When a matrix has an isotropic tangent constitutive tensor, namely one of the form

$$\mathbb{L}^{(1)} = 3k_t \mathbb{J} + 2\mu_t \mathbb{K},$$

where μ_t and k_t are shear and compressibility moduli, respectively, while $\mathbb{J}$ and $\mathbb{K}$ represent volumetric and deviatoric fourth-rank identity tensors, respectively, it is possible to determine an explicit form of Eshelby's tensor:

$$\mathbb{S}^E = \frac{3k_t}{3k_t + 4\mu_t}\mathbb{J} + \frac{6(k_t + 2\mu_t)}{5(3k_t + 4\mu_t)}\mathbb{K}.$$

If the porous spheres are randomly dispersed in the reference configuration, the macroscopic behavior of the composite can be considered isotropic at first glance. It is possible then to express shear and bulk moduli as

$$k_t = \mathbb{J} \cdot \mathbb{L}^{(1)}, \quad \mu_t = \frac{1}{5}\mathbb{K} \cdot \mathbb{L}^{(1)}. \tag{3.4}$$

The isotropic version $\mathbb{L}^{(1)}_{\text{iso}}$ of the tangent constitutive tensor follows and the isotropic version of the Eshelby tensor can be derived according to equation (3.2). It implies the isotropic version of Hill's tensor:

$$\mathbb{P}_{\text{iso}} = \mathbb{S}^E(\mathbb{L}^{(1)}_{\text{iso}})\mathbb{L}^{(1)^{-1}}. \tag{3.5}$$

When using equation (3.3) to update the value of $\overline{\mathbf{F}}^{(1)}$ at each iteration, only the two tangent shear and compressibility moduli can be explictly computed from equation (3.4), instead of integrating the 81 components of Hill's tensor (2.10).

In the presence of appropriate symmetries of the elastic tensor appropriate specific strategies for the evaluation of Hill's tensor components can be adopted (see, e.g., [75,76]).

4 Results and discussion

We show results for each nominal strain $1 - \overline{\lambda}$ in terms of $|\overline{\mathbf{P}}_{11}|$.

We refer to data from confined compression tests involving samples obtained by either adding microfluidic-based or double emulsion-based spheres into the polyol B part prior to incorporation of isocyanate A. Test structures (Figure 2), specimen dimensions and measurements are the same used to characterize the PU matrix.

We realized tests on two configurations of composite specimens with volume fraction of type C monodisperse microspheres (with $f_0 = 0.3$ in terms of porosity) amounting to $c^{(2)} = 0.02$ and 0.066, respectively (Figures 6 and 7).

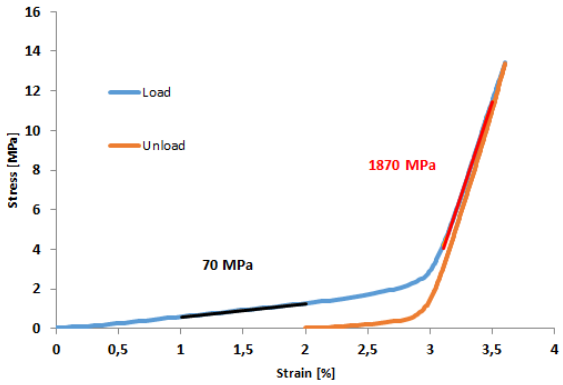

Figure 6. Confined compression test on 6.6% filled PU.

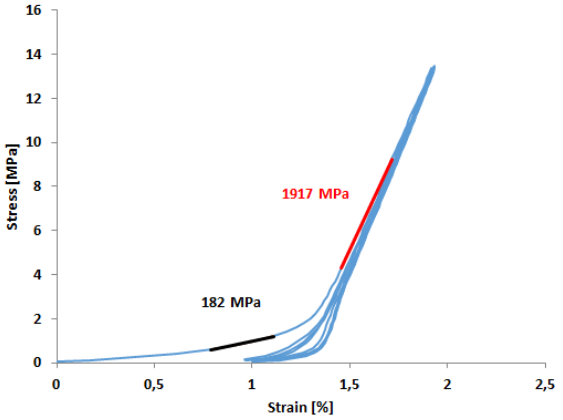

Figure 7. Confined compression test on 2% filled PU.

Figures 8 and 9 summarize results of the analytical homogenization process in confined compression state with $c^{(2)}$ corresponding to 6.6% and 2% volume fraction of porous spherical inclusions, respectively, obtained by directly integrating the Hill tensor. In both cases, the homogenization appears very accurate in small strain regime. As the imposed macroscopic deformation increases, the analytical evaluation overestimates the actual behavior. Actually, the result is an upper bound for a real behavior. The pertinent trend is adequately represented, considering the very limited available data concerning the constituents.

A comparison between results obtained through direct integration of equation (2.10) and those emerging after rendering isotropic the Hill tensor (3.5) appears in Figures 10 and 11. There is no significant discrepancy in the results. So, the process of rendering isotropic the Hill tensor can be conveniently exploited because it is simpler and faster than the full integration in formula (2.10).

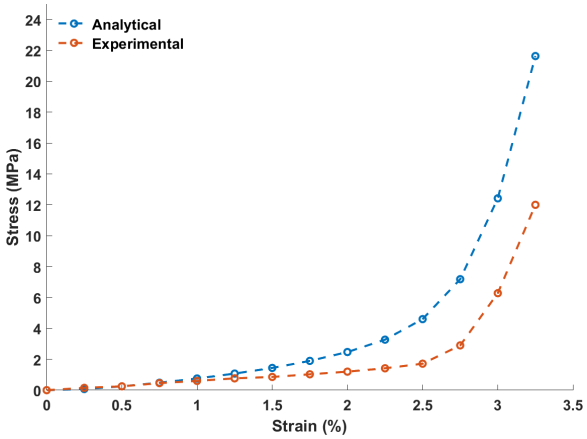

Figure 8. Comparison between experimental tests and analytical homogenization for PU with 6.6% porous inclusions.

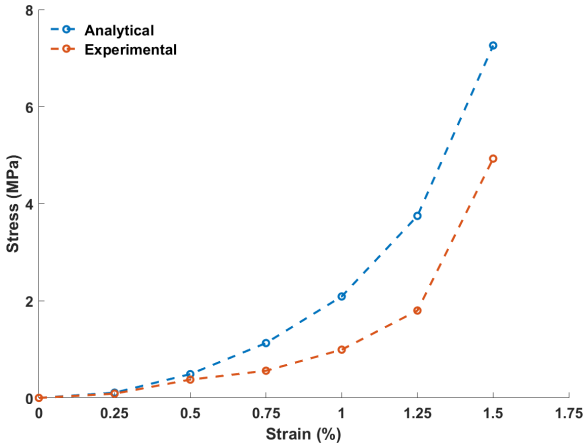

Figure 9. Comparison between experimental tests and analytical homogenization for PU with 2% porous inclusions.

4.1 Microstructural effects

Figure 12 shows the predicted trend of porosity f in the inclusions as a function of the applied macroscopic strain. The porosity in the inclusions, since the silicone is considered as incompressible, is simply calculated as (see also [58]):

$$f = \frac{J^{(2)} - 1 + f_0}{J^{(2)}} \,. \tag{4.1}$$

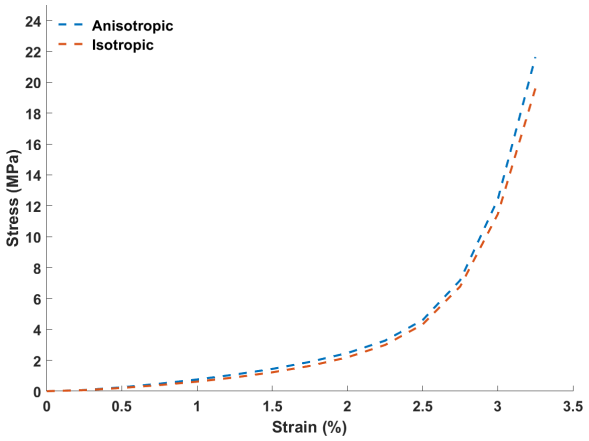

Figure 10. Comparison between the analytical result obtained with and without isotropization of Hill's tensor for PU with 6.6% porous inclusions.

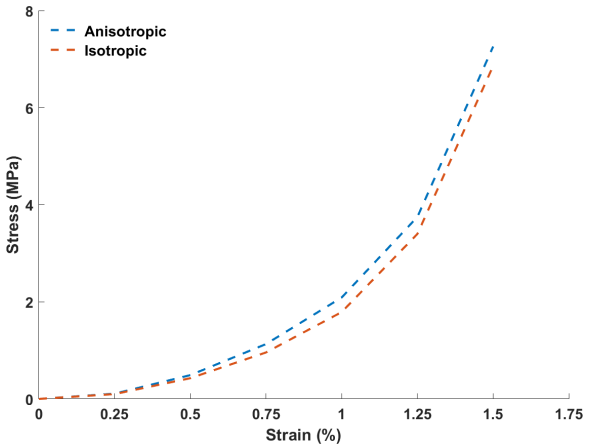

Figure 11. Comparison between the analytical result obtained with and without isotropization of Hill's tensor for PU with 2% porous inclusions.

The effective porosity is critical for applications; the acoustic properties strongly depend on actual porosity and size of the spheres, and only in appropriate optimal conditions there is resonance and therefore acoustic attenuation.

Figure 13 shows that the porous inclusions undergo volumetric changes much higher than the PU matrix, which is stiffer. In particular, the maximal volume variations of the matrix are around 1%. Such a value falls in the range where the chosen form of the PU elastic energy closely approximates the experimental behavior (see Figure 4).

5 Comparison with finite element simulations

We compare results obtained via the second-order truncation of the elastic energy Taylor's expansion used above with what emerges from a numerical

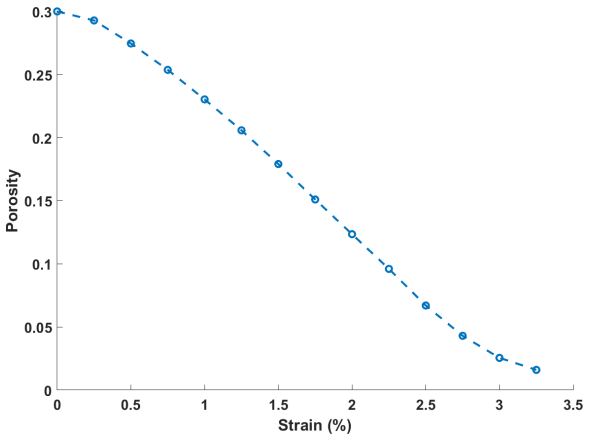

Figure 12. Variation of the porosity volume fraction in inclusions as a function of the applied macroscopic strain (6.6% filled PU): analytical estimate.

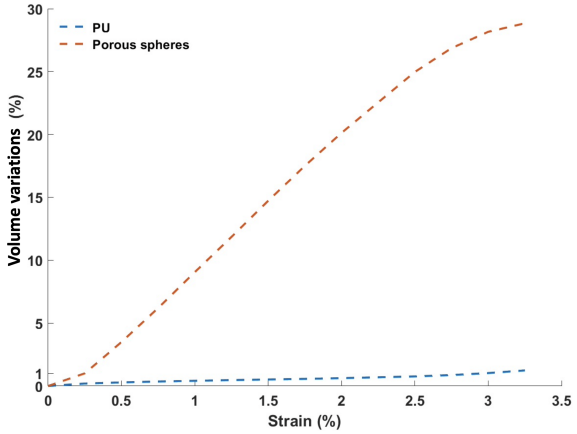

Figure 13. Analytical estimate of the volume variations $(1 - J^{(r)},\ r = 1, 2)$ in the PU matrix and in the inclusions, respectively (6.6% filled PU).

homogenization tested on the four classes of porous inclusions shown in Table 1. For such non-linear quasi-static analyses we used the commercial FE software ANSYS [2]. We include both material and geometrical non-linearity.

5.1 The finite element scheme adopted

We take a heterogeneous medium considered to be statistically periodic, with characteristic SRVE containing a random distribution of a sufficiently large number of inclusions. A Python script generates the SRVE, which consists of a cubic block containing non-overlapping spheres with diameters randomly chosen from the distributions listed in Table 1 and placements inside the block drawn from a uniform distribution (as shown in Figures 14 and 15).

A Yeoh-type strain energy density is assigned to the PU matrix, with the

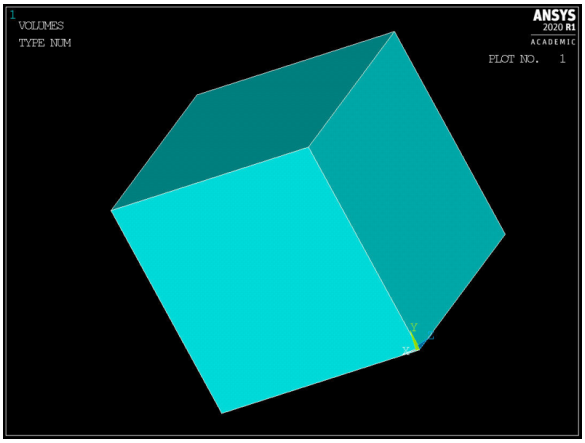

Figure 14. A picture of SRVE used for the FE simulations: matrix block.

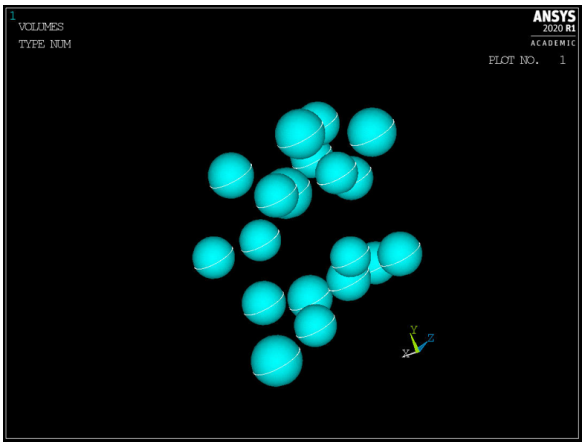

Figure 15. A picture of SRVE used for the FE simulations: inclusions.

parameters listed in the first row of Table 2, and the elastic energy density (2.1) is assigned to the inclusions by means of a USERMAT subroutine [3]. ANSYS SOLID186 elements, with 20 nodes and 3 degrees of freedom per node, model both phases constrained by mesh continuity at the matrix-sphere interface. In other words, we assume a perfect adhesion between matrix and inclusions. Also, the SRVE undergoes Dirichlet's conditions at the boundary nodes, namely

$$\mathbf{u}_i = (\overline{\mathbf{F}} - \mathbf{I})\mathbf{x}_i, \quad i = 1, ..., N_b, \tag{5.1}$$

where N_b is the total number of nodes located on the boundary of the SRVE and $\mathbf{x}_i = (x_i, y_i, z_i)$ is the position of the i-th node in the global frame chosen in the reference configuration. $\overline{\mathbf{F}}$ is the one in equation (3.1). It refers to 3.25% compression strain ($\overline{\lambda} = 0.9675$). Specifically, the prescribed boundary conditions on the i-th node are $u_y = u_z = 0$ and $u_x = -0.0325x_i$. The lower face of the block, along the compression direction x, has been placed in the plane $x = 0$, so that the nodal degrees of freedom at $x = 0$ (in the reference configuration) are equal to zero in order to avoid a rigid displacement of the SRVE.

5.2 Results and comparisons

We investigated the numerical sensitivity to both SRVE size l and mesh average element size for type A monodisperse spheres. Coarse, average, and fine discretization types have been defined by varying the LESIZE control parameter (which defines the element size) as a function of side block length l and mean inclusion radius R, as reported in Table 4 and shown in Figure 16 for the porous spherical inclusions. For each discretization level, the overall number of elements composing the FE model is reported in Table 4. As expected, an average discretization represents a good compromise between accuracy and computational cost. Figures 17 and 18 show the results of the sensitivity analysis.

A second sensitivity analysis aimed at investigating the influence of the SRVE characteristic size l and the number of inclusions into the SRVE, on the overall macroscopic response. For the sake of brevity, we performed this analysis only for the "average" discretization type indicated in Table 4. Three different values of l have been considered, as shown in Table 5. Figures 19 and 20 show the pertinent results. No appreciable difference appears between the considered SRVE sizes, as they account for an adequate number of dispersed inclusions. In fact, at least 25 embedded spheres have been deemed to be enough for our analyses. Therefore, we have considered such a configuration (i.e., "average" discretization and at least 25 inclusions) in the remaining analyses because it ensures sufficiently accurate results in a reasonable computational time with an overall (almost) isotropic elastic response of the body.

Discretization	n. elements	LESIZE block	LESIZE inclusions
coarse	45.000	$l/10$	$R/10$
average	100.000	$l/15$	$R/15$
fine	200.000	$l/20$	$R/20$

Table 4
Mesh discretization sensitivity parameters.

Block length l (mm)	n. inclusions
1	19
1.25	33
1.5	57

Table 5
SRVE size sensitivity.

Figures 21-to-24 summarize analytical and numerical results obtained under confined compression for the four types of considered inclusions and a PU ma-

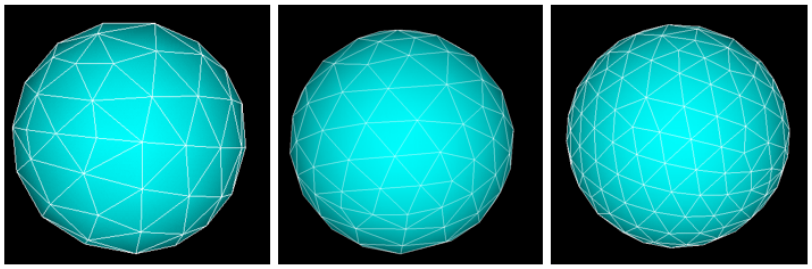

Figure 16. Detail of discretization on spherical inclusions. From left to right: coarse, medium and fine discretizations.

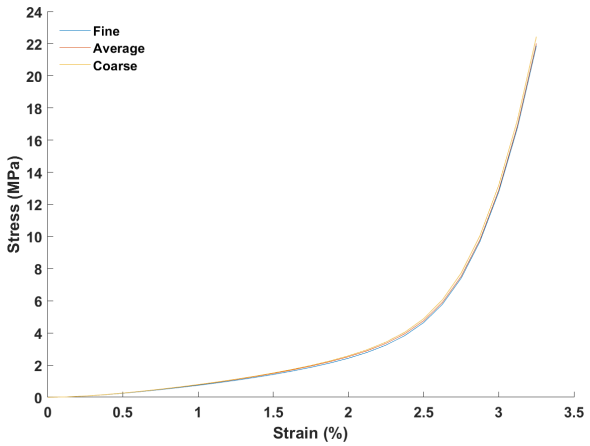

Figure 17. Mesh density sensitivity analysis on a SRVE of side length 1 mm with 6.6% of type A spherical inclusions: stress-strain relationship. (Type A monodisperse spheres.)

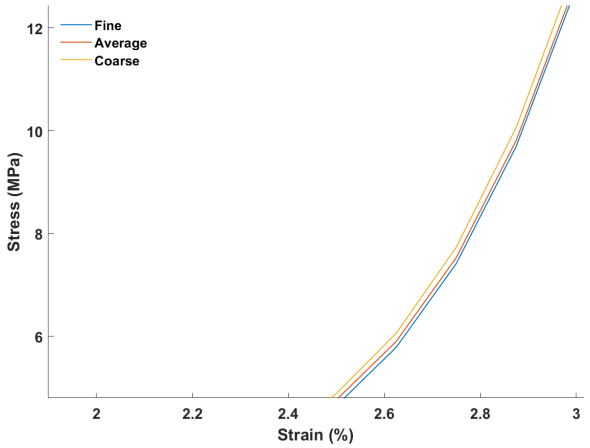

Figure 18. Mesh density sensitivity analysis on a SRVE of side length 1 mm with 6.6% of type A spherical inclusions: detail of stress-strain relationship. (Type B monodisperse spheres.)

trix filled by spheres up to 6.6% of its volume. The curve relative to numerical FE results represents the average of 3 tests realized on 3 SRVEs having different random distributions of inclusions. Analytical predictions are in close

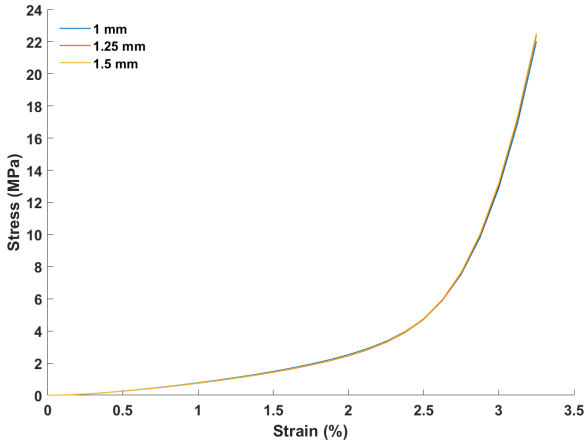

Figure 19. SRVE size sensitivty analysis for SRVEs with 6.6% of type A spherical inclusions with average mesh density: stress-strain relationship.

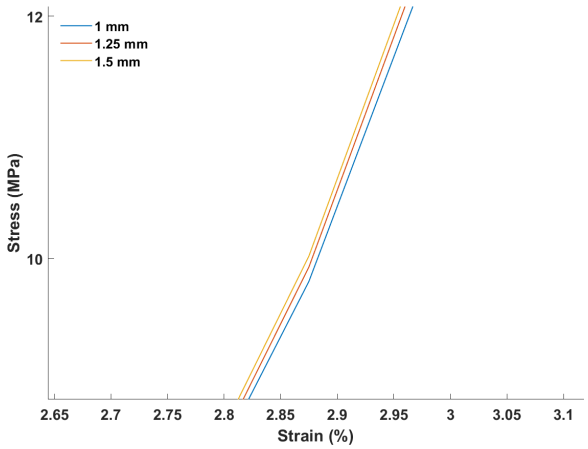

Figure 20. SRVE size sensitivty analysis for SRVEs with 6.6% of type A spherical inclusions with average mesh density: detail of stress-strain relationship.

agreement with the numerical results, for various dimensions of the porous spherical inclusions. The proposed analytical homogenization appears to be independent of the actual inclusion size, but it depends on their volume fraction. More recent works based on an approximate solution for non-Gaussian rubber reinforced by an isotropic distribution of rigid particles [37,19], show, as well, this size insensitivity effect. This is in agreement, also, with other results available in the pertinent literature [18,55,54,62].

Some discrepancies can be observed with experimental results illustrated in Figures 6 and 7. This is due to various factors. First, experiments are performed on a specimen characterized by the geometrical parameters presented in Section 4, under confined compression, while numerical and analytical results refer to a SRVE subjected to the same macroscopic deformation, assumed to be uniform, measured during the experimental test. Of course, both FE model and analytical approach do not take into account boundary phenomena arising from non-ideal test conditions (e.g. friction and/or backlash

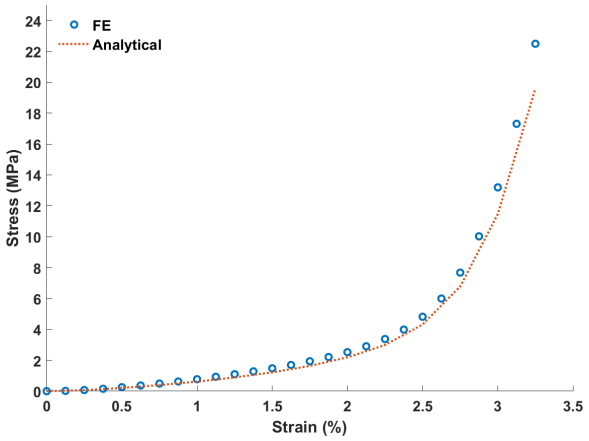

Figure 21. Type A monodisperse spheres: comparison between numerical and analytical results for 6.6% filled PU.

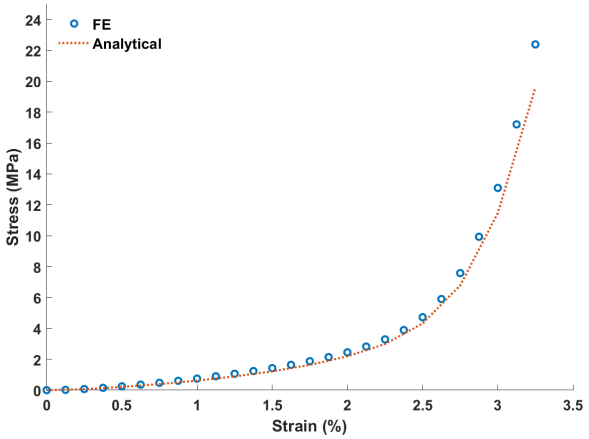

Figure 22. Type B monodisperse spheres: comparison between numerical and analytical results for 6.6% filled PU.

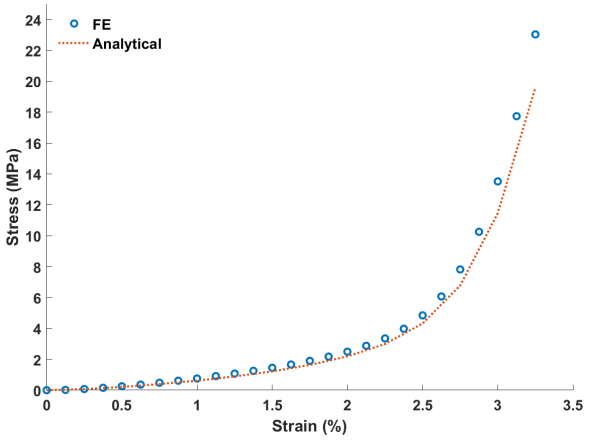

Figure 23. Type C monodisperse spheres: comparison between numerical and analytical results for 6.6% filled PU.

between specimen and container walls) and the specimen finite size. Also, the

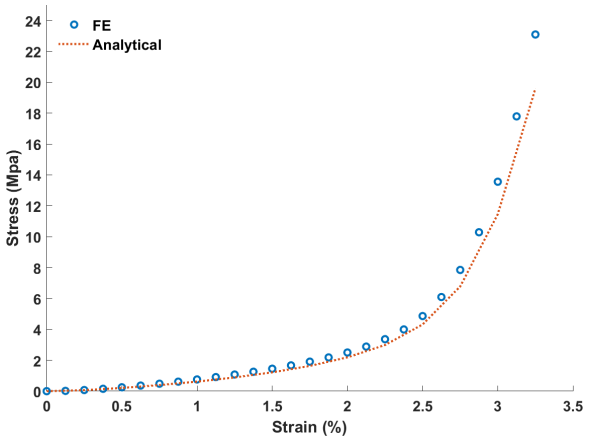

Figure 24. Type D polydisperse spheres: comparison between numerical and analytical results for 6.6 % filled PU.

assumption of perfect adherence between matrix and inclusions is only a rough approximation of reality wherein relative sliding may occur at the interfaces. Finally, the behavior of the PU matrix used in the FE analysis and in the analytical homogenization method is not in agreement with the real behavior of the elastomer, due to the possible presence of defects like micro-porosities, which could influence its macroscopic response. The circumstance can be easily inferred from the analysis shown in Figures 8 and 9: the lower the volume fraction of spherical inclusions the higher a discrepancy between analytical and experimental results.

6 Final remarks

The two-level non-linear static homogenization analysis that we presented here appears to be adequate for two-phase composites wherein one of the two phases requires to be homogenized *per se*, as it occurs for the composite here considered: a material made of a polyurethane matrix filled by porous spherical inclusions.

Its physical properties are strongly affected by the finite strain state reached. Its peculiar structure suggests a low-scale homogenization (the one of spheres) followed by a second step that couples with a different method (the one based on a second-order truncation of the elastic energy Taylor's expansion) matrix and inclusions.

Our analytical and numerical results appear to be in good agreement with the experimental ones up to a strain lower than or equal to 1% in the confined compression test. Beyond such a range, high discrepancy with experiments can be observed. This is mainly due to the unavoidable differences existing between

an homogenization scheme, based on idealized boundary conditions, and what is experienced by real specimens. A more accurate characterization of the constituent phase material properties (i.e. a wider experimental campaign), together with a more pertinent boundary conditions to be imposed during the homogenization procedure, could lead to a better estimate, even beyond the limits envisaged here.

Moreover, as a future perspective of this work, according to the acoustic application of the considered composite, the provided results could be used as a starting configuration (pre-stress due to hydrostatic pressure of the water) to analyse the under-water furtivity performances of the material.

Acknowledgements. This work rests on ANR and DGA funding through the PANAMA Project (ANR-17-ASTR-0002). Also, P.-M. Mariano acknowledges GNFM-INDAM.

References

[1] Abbadi A., Koutsawa Y., Carmasol A., Belouettar S., Azari Z. (2019), Experimental and numerical characterization of honeycomb sandwich composite panels, **17**, 1533-1547.

[2] ANSYS (2020), *ANSYS mechanical APDL theory reference*, ANSYS Inc.

[3] ANSYS (2020), *ANSYS mechanical APDL programmers reference*, ANSYS Inc.

[4] Ba A., Kovalenko A., Aristégui C., Mondain-Monval O., Brunet T. (2017), Soft porous silicone rubbers with ultra-low sound speeds in acoustic metamaterials, *Sci. Reports*, **7**, 1-6.

[5] Baird A. M., Kerr F. H., Townend D. J. (1999), Wave propagation in a viscoelastic medium containing fluid-filled microspheres, *J. Acoust. Soc. America*, **105**, 1527-1538.

[6] Blatz P. J., Ko W. L. (1962), Application of finite elastic theory to the deformation of rubbery materials, *Trans. Soc. Rheology*, **6**, 223-252.

[7] Brunet T., Leng J., Mondain-Monval O. (2013), Soft acoustic metamaterials, *Science*, **342**, 323-324.

[8] Brunet T., Merlin A., Mascaro B., Zimny K., Leng J., Poncelet O., Aristegui C., Mondain-Monval O. (2015), Soft 3D acoustic metamaterial with negative index, *Nature Materials*, **14**, 384-388.

[9] Cappelli L., Montemurro M., Dau F., Guillaumat L. (2018), Characterisation of composite elastic properties by means of a multi-scale two-level inverse approach, *Comp. Struct.* **204**, 767-777.

[10] Cappelli L., Montemurro M., Dau F., Guillaumat L. (2019), Multi-scale identification of the viscoelastic behaviour of composite materials through a non-destructive test, *Mech. Mat.*, **137**, art. n. 103137.

[11] Cummer S. A., Christensen J., Alù A. (2016), Controlling sound with acoustic metamaterials, *Nature Rev. Mat.*, **1**, 1-13.

[12] Danielsson M., Parks D. M., Boyce M. C. (2004), Constitutive modeling of porous hyperelastic materials, *Mech. Mat.*, **36**, 347-358.

[13] Drugan W. J., Willis J. R. (1996), A micromechanics-based nonlocal constitutive equation and estimates of representative volume element size for elastic composites, *J. Mech. Phys. Solids*, **44**, 497-524.

[14] Elkem, `https://www.elkem.com/`.

[15] Eshelby J. D. (1957), The determination of the elastic field of an ellipsoidal inclusion, and related problems, *Proc. Royal Soc. London A*, **241**, 376-396.

[16] Fu S. Y., Lauke B. (1997), Analysis of mechanical properties of injection molded short glass fibre (SGF)/calcite/ABS composites, *J. of Materials Science and Technology*, **13**, 389-396.

[17] Geers M. G. D., Kouznetsova V. G., Brekelmans W. A. M. (2010), Multi-scale computational homogenization: Trends and challenges, *J. Comp. Appl. Math.*, **234**, 2175-2182.

[18] Gentieu T., Catapano A., Jumel J., Broughton J. (2019), A mean-field homogenisation scheme with CZM-based interfaces describing progressive inclusions debonding, *Comp. Struct.*, **229**, art. n. 111398.

[19] Goudarzi T., Spring D.W., Paulino G.H., Lopez-Pamies O. (2015), Filled elastomers: A theory of filler reinforcement based on hydrodynamic and interphasial effects, *J. of the Mechanics and Physics of Solids*, **80**, 37-67.

[20] Haberman M. R., Guild M. D. (2016), Acoustic metamaterials, *Phys. Today*, **69**, 42-48.

[21] Hashin Z. (1962), The elastic moduli of heterogeneous materials, *ASME J. Appl. Mech.*, **29**, 143-150.

[22] Hashin Z., Shtrikman S. (1962), On some variational principles in anisotropic and nonhomogeneous elasticity, *J. Mech. Phys. Solids*, **10**, 335-342.

[23] Hashin Z. (1985), Large isotropic elastic deformation of composites and porous media, *Int. J. Solids Struct.*, **21**, 711-720.

[24] Hill R. (1963), Elastic properties of reinforced solids: some theoretical principles, *J. Mech. Phys. Solids*, **11**, 357-372.

[25] Hill R. (1965), Continuum micro-mechanics of elastoplastic polycrystals, *J. Mech. Phys. Solids*, **13**, 89-101.

[26] Hill R. (1972), On constitutive macro-variables for heterogeneous solids at finite strain, *Proc. Royal Soc. London A*, **326**, 131-147.

[27] Hill R., Rice J. (1973), Elastic potentials and the structure of inelastic constitutive laws, SIAM emphJ. Appl. Math., **25**, 448-461.

[28] Kanit T., Forest S., Galliet I., Mounoury V., Jeulin D. (2003), Determination of the size of the representative volume element for random composites: statistical and numerical approach, *Int. J. Solids Struct.*, **40**, 3647-3679.

[29] Krajcinovic D. (1996), *Damage mechanics*, North-Holland, Amsterdam.

[30] Landauer A. K., Li X., Franck C., Henann D. L. (2019), Experimental characterization and hyperelastic constitutive modeling of open-cell elastomeric foams, *J. of the Mechanics and Physics of Solids*, **133**, 103701.

[31] Lazzeri A., Thio Y. S., Cohen R. E. (2004), Volume strain measurements on CaCO3/polypropylene particulate composites: the effect of particle size, *J. of Applied Polymer Science*, **91**, 925-935.

[32] Levin V. M. (1967), Thermal expansion coefficients of heterogeneous materials, *Mech. Solids*, **21**, 9–17.

[33] Li Y., Yu G., Liang B., Zou X., Li G., Cheng S., Cheng J. (2014), Three-dimensional ultrathin planar lenses by acoustic metamaterials, *Scient. Rep.*, **4**, 1-6.

[34] Liu W. K., Karpov E. G., Zhang S., Park H. S. (2004), An introduction to computational nanomechanics and materials, *Comp. Meth. Appl. Mech. Eng.*, **193**, 1529-1578.

[35] Lopez-Pamies
O., Ponte-Castañeda P. (2007), Homogenization-based constitutive models for porous elastomers and implications for macroscopic instabilities: I- Analysis, *J. Mech. Phys. Solids*, **55**, 1677-1701.

[36] Lopez-Pamies
O., Ponte-Castañeda P. (2007), Homogenization-based constitutive models for porous elastomers and implications for macroscopic instabilities: II—Results, *J. Mech. Phys. Solids*, **55**, 1702-1728.

[37] Lopez-Pamies O., Goudarzi T., Danas K. (2013), The nonlinear elastic response of suspensions of rigid inclusions in rubber: II — A simple explicit approximation for finite-concentration suspensions, *J. Mech. Phys. Solids*, **61**, 19-37.

[38] Matis B. R., Liskey S. W., Gangemi N. T., Waters Z. J., Edmunds A. D., Wilson W. B., Photiadis D. M., Houston B. H., Baldwin J. W. (2020), Critical role of a nanometer-scale microballoon shell on bulk acoustic properties of doped soft matter, *Langmuir*, **36**, 5787-5792.

[39] Mariano P. M. (2002), Multifield theories in mechanics of solids, *Adv. Appl. Mech.*, **38**, 1-93.

[40] Mariano P. M., Stazi F. L. (2005), Computational aspects of the mechanics of complex materials, *Arch. Comp. Methods Eng.*, **12**, 391-478.

[41] Mariano P. M., Gioffrè M., Stazi F. L., Augusti G. (2004), Elastic microcracked bodies with random properties, *Prob. Eng. Mech.*, **19**, 127-143.

[42] Miehe C., Schröder J., Schotte J. (1999), Computational homogenization analysis in finite plasticity simulation of texture development in polycrystalline materials, *Comp. Meth. Appl. Mech. Eng.*, **171**, 387-418.

[43] Milton G. W. (2002), *The theory of composites*, Cambridge University Press, Cambridge.

[44] Naify C. J., Martin T. P., Layman C. N., Nicholas M., Thangawng A. L., Calvo D. C., Orris G. J. (2014), Underwater acoustic omnidirectional absorber, *Appl. Phys. Lett.*, **104**, art. n. 073505.

[45] Ogden W. R. (1974), On the overall moduli of non-linear elastic composite materials, *J. Mech. Phys. Solids*, **22**, 541-553.

[46] Ogden R. W. (1978), Extremum principles in non-linear elasticity and their application to composites—I: Theory, *14*, 265-282.

[47] Ponte-Castañeda P. (1989), The overall constitutive behaviour of non-linearly elastic composites, *Proc. Royal Soc. London A*, **422**, 147-171.

[48] Ponte-Castañeda P. (1991), The effective mechanical properties of non-linear isotropic composites, *J. Mech. Phys. Solids*, **39**, 45-71.

[49] Ponte-Castañeda P. (1996), Exact second-order estimates for the effective mechanical properties of non-linear composite materials, *J. Mech. Phys. Solids*, **44**, 827-862.

[50] Ponte-Castañeda P. (2002), Second-order homogenization estimates for non-linear composites incorporating field fluctuations: I—Theory, *J. Mech. Phys. Solids*, **50**, 737-757.

[51] Ponte-Castañeda P. (2002), Second-order homogenization estimates for non-linear composites incorporating field fluctuations: II—Applications, *J. Mech. Phys. Solids*, **50**, 759-782.

[52] Ponte-Castañeda P., Tiberio E. (2000), A second-order homogenization method in finite elasticity and applications to black-filled elastomers, *J. Mech. Phys. Solids*, **48**, 1389-1411.

[53] Poupart R., Lacour T., Darnige P., Poncelet O., Aristégui C., Voisin T., Marre S., Brunet T., Mondain-Monval O. (2020), Elaboration of soft porous ultrasound insulators, *RSC Advances*, **10**, 41946-41953.

[54] Radford K. C. (1971), The mechanical properties of an epoxy resin with a second phase dispersion, *J. Mat. Sci.*, **6**, 1286-1291.

[55] Shah, A. ur R., Lee D., Wang Y., Wasy A., Ham K., Jayaraman K., Kim B.-S., Song J.-I. (2014), Effect of concentration of ATH on mechanical properties of polypropylene/aluminium trihydrate (PP/ATH) composite, *Trans. Nonferrous Metals Soc. China*, **24**, s81-s89.

[56] Shao-Yun F., Xi-Qiao F., Bernd L., Yiu-Wing M. (2008), Effects of particle size, particle/matrix interface adhesion and particle loading on mechanical properties of particulate–polymer composites, *Composites Part B: Eng.*, **39**, 933-961.

[57] Shin H. D., Ahn B. H. (2017), Study on the underwater acoustic properties of polyurethane elastomer, *Rubber Soc. Korea*, **52**, 326-331.

[58] Shrimali B., Lefèvre V., Lopez-Pamies O. (2019), A simple explicit homogenization solution for the macroscopic elastic response of isotropic porous elastomers, *J. Mech. Phys. Solids*, **122**, 364-380.

[59] Shrimali B., Parnell W.J., Lopez-Pamies O. (2020), A simple explicit model constructed from a homogenization solution for the large-strain mechanical response of elastomeric syntactic foams, *Int. J. of Non-Linear Mechanics*, **126**, 103548.

[60] M. Šilhavý, *The mechanics and thermodynamics of continuous media*, Springer-Verlag, Berlin, 1997.

[61] Sika, `https://www.sika.com/`.

[62] Singh R. P., Zhang M., Chan D. (2002), Toughening of a brittle thermosetting polymer: effects of reinforcement particle size and volume fraction, *J. Mat. Sci.*, **37**, 781-788.

[63] Spanoudakis J., Young R. J. (1984), Crack propagation in a glass particle-filled epoxy resin. Part 1: Effect of particle volume fraction and size, *J. of Materials Science*, **19**, 473-486.

[64] Sperling L. H. (1990), Sound and vibration damping with polymers: Basic viscoelastic definitions and concepts, *ACS Publications*, available at `https://pubs.acs.org/doi/pdf/10.1021/bk-⊂1990-⊂0424.ch001`

[65] Suprapakorn N., Dhamrongvaraporn S. S. (1998), Effect of $CaCO_3$ on the mechanical and rheological properties of a ring-opening phenolic resin: polybenzoxazine, *Polymer Composites*, **19**, 126-132.

[66] Suquet P. M. (1985), Elements of homogenization for inelastic solid mechanics, in *Homogenization Techniques for Composite Media*, Lecture Notes in Physics, **272**, Springer-Verlag, Berlin.

[67] Suquet P., Ponte-Castañeda P. (1998), non-linear composites, *Adv. Appl. Mech.*, **34**, 171-302.

[68] Willis J. R. (1981), Variational and related methods for the overall properties of composites, *Adv. Appl. Mech.*, **21**, 1-78.

[69] Yeoh O. H. (1993), Some forms of the strain energy function for rubber, *Rubber Chem. Tech.*, **66**, 754-771.

[70] Yoshinobu N., Miho Y., Masayoshi O., Tsunetaka M. (1992), Effects of particle size on mechanical and impact properties of epoxy resin filled with spherical silica, *J. of Applied Polymer Science*, **45**, 1281-1289.

[71] Yu W., Tang T. (2007), Variational asymptotic method for unit cell homogenization of periodically heterogeneous materials, *Int. J. Solids Struct.*, **44**, 3758-3775.

[72] Zhang Q., Tian M., Wu Y., Lin G., and Zhang L. (2004), Effect of particle size on the properties of $Mg(OH)_2$-filled rubber composites, *J. of Applied Polymer Science*, **94**, 2341-2346.

[73] Zhang C. H., Hu Z., Gao G., Zhao S., Huang Y. D. (2013), Damping behavior and acoustic performance of polyurethane/lead zirconate titanate ceramic composites, *Mat. Design*, **46**, 503-510.

[74] Zhou H., Li B., Huang G. (2006), Sound absorption characteristics of polymer microparticles, *J. App. Polymer Sci.*, **101**, 2675-2679.

[75] Walpole L.J. (1984), Fourth-rank tensors of the thirty-two crystal classes: multiplication tables, *Proc. R. Soc. Lond. A*, **391**, 149-179.

[76] Barthélémy J.F. (2020), Simplified approach to the derivation of the relationship between Hill polarization tensors of transformed problems and applications, *Int. J. of Engineering Science*, **154**.